

Oxygen-containing groups in cellulose- and lignin-biochar: their roles in U(VI) adsorption

Jianjun Liang (✉ liangjj@lzb.ac.cn)

Northwest Institute of Eco-Environment and Resources <https://orcid.org/0000-0003-3233-1368>

Yongzhong Feng

Gansu province land development and rehabilitation center

Xiaoyi Qiu

Gansu province land development and rehabilitation center

Zhuolin Tao

Gansu province land development and rehabilitation center

Zhengyang E

Northwest Institute of Eco-Environment and Resources

Jiayu Song

Northwest Institute of Eco-Environment and Resources

Yaqiong Dong

Northwest Institute of Eco-Environment and Resources

Ping Li

Northwest Institute of Eco-Environment and Resources

Qiaohui Fan

Northwest Institute of Eco-Environment and Resources

Research Article

Keywords: Biochar, Lignin, Cellulose, Uranium, Oxygen-containing groups, Adsorption

Posted Date: March 28th, 2022

DOI: <https://doi.org/10.21203/rs.3.rs-1421364/v1>

License:   This work is licensed under a Creative Commons Attribution 4.0 International License.

[Read Full License](#)

Abstract

The adsorption behaviors of cellulose- and lignin-biochar depend on their oxygen-containing groups to some extent. In this study, a series of cellulose- and lignin-rich biochar was prepared from pakchoi and corncob, respectively named PBC and CBC, to evaluate their adsorption properties for U(VI). The maximal adsorption capacity of PBC 300 (obtained at 300 °C) was 46.62 mg g⁻¹ for U(VI), which was 1.3 times higher than that of CBC 300 (35.60 mg g⁻¹). U(VI) adsorption on PBC and CBC were ascribed to the coordination interaction between oxygen-containing groups and U(VI). Interestingly, the main complexation groups were different in the both biochar due to the inherent evolution of cellulose and lignin. Volatile d-glucose chains in cellulose were apt to degrade rapidly, and the formed carboxyls acted as the main adsorption sites in PBC. However, the stable aromatic network in lignin led to a slow degradation, and more hydroxyls thus remained in CBC, which controlled U(VI) adsorption. This study obtained effective adsorbents of U(VI) and provided some essential insights into understanding this evolution and structure-function relationship of biochar.

1 Introduction

Uranium is regarded as one of the most important radionuclides (Karim et al., 2016; Liu et al., 2017; J. Wang et al., 2020a) in the whole nuclear industry (Wen et al., 2016; Wang et al., 2020). Once released into the environment, hexavalent U(VI) would result in a horrible threat to ecological safety and human health due to its high radioactive and chemical toxicities (Li et al., 2019; Li et al., 2019b). Therefore, the efficient removal of U(VI) from the polluted water is urgent and desirable. Numerous techniques have been adapted for U(VI) removal, such as adsorption (Li et al., 2019; Philippou et al., 2019), chemical precipitation (Foster et al., 2019), ion exchange (Cheng et al., 2019), photocatalysis (Wang et al., 2020b), and solvent extraction (Prabhu et al., 2017), and so on. Among these techniques, the adsorption promises the most feasible approach owing to its cost-effective advantage and convenient operation (Ahmed et al., 2021a, 2021d).

To date, a large number of adsorbents have been designed for U(VI) separations, including zeolites (Wu et al., 2019), minerals (Liu et al., 2017), artificial materials, and so on. By comparison, biochar proves a promising application because of its low cost, huge surface area, and superior stability (Inyang et al., 2016; Ahmed et al., 2021c). Various biochar has shown excellent adsorption capacities for U(VI) pollutants (Liu et al., 2017; Li et al., 2019; Ahmed et al., 2021b). The in-depth researches suggest that the adsorption performance of biochar depends on their chemical compositions, microstructures, and preparation methods (Enders et al., 2012; Suliman et al., 2016; Yoon et al., 2019). As the major biomasses, cellulose and lignin control the structures and functions of the resulting biochar to some extent (Li et al., 2014). It is important to illuminate the microstructural evolution of cellulose and lignin during the pyrolysis procedure, in particular, their oxygen-containing group transformations.

Cellulose is mainly composed of regular D-glucose chains with β -1,4 glycosidic connections, and thus shows the chemical characters of alkyl alcohol and ether (Raap et al., 2019; He et al., 2020; Zhao et al.,

2019; Cheng et al., 2021). Lignin is usually regarded as a complicated three-dimensional network constructed by both aliphatic and aromatic polymer, where phenylpropane, interconnected by ether bonds, is the major units (Sharma et al., 2004; Kijima et al., 2011; Meng et al., 2021). As heated in nitrogen or inert atmosphere, cellulose and lignin experience a series of complicated deoxidation reactions (Bradbury and Shafizadeh, 1980), as well as polyaromatic crosslinking and stack (Ishimaru et al., 2007). Due to the aliphatic feature, cellulose readily decomposes and transforms at a relatively low temperature²⁹. During 300–400 °C, the pyrolysis of cellulose involved the rearrangement and oxidation of C = C, C = O, COO, paraffinic, aromatic groups, etc. (Shafizadeh and Sekiguchi, 1984). As the main substructure, the glycosyl units decompose rapidly to levoglucosan (Shafizadeh et al., 1979). Meanwhile, the aliphatic chains in cellulose entangle irregularly, resulting in abundant disordered structures (Bradbury et al., 1979; Shafizadeh and Lai, 1975). By contrast, lignin is more stable, and slowly decomposes at a much wider range (160–900 °C) (Sharma et al., 2004). Above 400 °C, plenty of CO₂, CO, CH₄, furan, methanol, and large-molecule volatiles are released due to the breakage of the C-O bond, C = O, -OCH₃, and -CH₂ (Suzuki et al., 2001) in lignin (Cao et al., 2013). Consequently, the formed lignin carbon shows stronger stability than cellulose carbon because of its higher content of aromatic structures (Xie et al., 2009).

These variable structures lead to significant differences in the adsorption behaviors of cellulose- and lignin-biochar. Cellulose-biochar shows stronger Cd(II) enrichment ability than lignin-biochar, because its plentiful mesopores provide effective channels to facilitate the pollutant penetrations, and abundant oxygen-containing groups guarantee large numbers of lone pair electrons to coordinate with Cd(II) ions (Chen et al., 2018). Sawdust biochar, which remains abundant cellulose, can remove heavy metals effectively due to the negatively charged surface and a large quantity of oxygen-containing groups (Komnitsas et al., 2016). In comparison, Pb(II) immobilization on lignin-biochar is proved a competitive method due to its fast mineral precipitation and surface complexation (Wu et al., 2021). For anionic pollutants, lignin-biochar can also provide efficient hydrogen bond sites and beneficial surficial electrostatic attraction (Yoon et al., 2019). To date, biochar from various precursors has been extensively explored to elucidate their surface characteristics and adsorption properties. However, the inherent differences in cellulose- and lignin-biochar are still scarcely discussed, especially, their adsorption sites and immobilization mechanisms. Moreover, U(VI) sequestration on biochar is also rarely reported.

In this study, we chose cellulose-rich pakchoi biochar (PBC) and lignin-rich corncob biochar (CBC) as adsorbents to explore their adsorption behavior for U(VI). A series of PBC and CBC were prepared via charring at 300, 400, and 500 °C, respectively. The obtained biochar was thus donated as PBC 300, PBC 400, PBC 500, CBC 300, CBC 400, and CBC 500, respectively. Batch experiments were performed to evaluate and compare the adsorption kinetics of U(VI) on PBC and CBC. The corresponding mechanisms were revealed via spectroscopic measurements. These findings about cellulose and lignin carbon are important for the practical application of biochar in the sequestration of U(VI).

2 Materials And Methods

2.1 Materials

Uranium nitrate ($\text{UO}_2(\text{NO}_3)_2 \cdot 6\text{H}_2\text{O}$) was purchased from Jieke chemapol and was dissolved in the Milli-Q water (18.2 M Ω) to prepare U(VI) stock solution. All chemicals in the subsequent experiments were of analytical grade and used without further purification. The preparation method and characterization of biochar were described in Appendix A Text S1 & S2.

2.2 Adsorption experiments

The biochar adsorbent was added into the tubes, making the mass-to-volume ratio (m/v) equal to 0.3 $\text{g} \cdot \text{L}^{-1}$. The effect of the pH values was studied at constant uranium concentration of 10^{-5} M and NaCl background electrolyte of 0.01M. Milli-Q water was injected to maintain the total volume of 8.0 mL. The pH values of the suspension were adjusted by dropping a negligible volume of HCl and/or NaOH solution, and then was shaken at 150 rpm. At pre-set time intervals, the dispersion was partially collected and filtered with a 0.22 μm membrane. The concentration of U(VI) in the filtrates was measured using spectrophotometry at 652 nm with arsenazo III as chromogenic reagent (Li et al., 2019a). The corresponding calculations were stated in Appendix A Text S3. including the adsorption rate of U(VI) and the simulations of the kinetics.

Regeneration and recycling experiments were conducted to investigate the stability of PBC and CBC in the environment. 40 mL Na_2CO_3 solutions (0.1 M), acted as eluent, were injected to adsorption-equilibrium PBC and CBC (12 mg) to desorb the loading U(VI). The sample was shaking for an hour, and then filtered. The U(VI) concentration was measured with the above method. The processes repeated six cycles to evaluate the stability of PBC and CBC.

3 Results And Discussion

3.1 Characterization

The microscopic morphologies have been recorded for PBC and CBC prepared at the variable temperatures, respectively. As shown in Figs. 1a and 1c, PBC displayed multilevel fibrous porous that spread in the whole framework regularly. PBC 300 showed a rough surface. Compared with PBC 300, the regular and loose pores were further developed in the PBC 400 and PBC 500 due to the pyrolysis of cellulose. For CBC, irregular folds constructed large quantities of disordered channels, and small carbon sphere particles were observed on their surface (Figs. 1d and 1f). The blurred pores and broken fragments were observed in CBC 500 owing to the deterioration of the carbon skeleton at the high pyrolysis temperature. These characteristic morphologies were consistent with previous findings (Ahmed et al., 2021d).

There were obvious differences in the surficial oxygen-containing functional groups of cellulose-rich PBC and lignin-rich CBC (Figs. 2a and 2b). PBC 300 showed a quite strong band at $\sim 1593 \text{ cm}^{-1}$ with a broad halfwidth, which could be assigned to a combined band of $\nu(\text{C}=\text{O})$ and $\nu(\text{C}=\text{C})$ (Zhang et al., 2021).

Meanwhile, a weak vibration was observed at 1031 cm^{-1} ascribed to $\nu(\text{C-O-C})$ (Li et al., 2019). These bands indicated a high content of carbonyls and carboxyls, but much less ether groups in PBC 300. In fact, the difference of oxygen-containing groups could be ascribed to unstable D-glucose chains in cellulose. The complicated chemical reactions during the hydrolyzation possibly caused the crack of β -1,4 glycosidic connections resulting in a decreasing ether content. Simultaneously, a large number of hydroxyls were oxidized into carbonyls and carboxyls (Meng et al., 2021). This hypothesis could be proved by the analysis of XPS. In the O 1s spectrum of PBC 300 (Fig. 2c), two peaks could be observed including a strong peak at 531.2 eV and another tiny one at 533.3 eV, which corresponded to C = O and C-O moieties, respectively (Xu et al., 2020). The great difference in the integral areas indicated that PBC 300 had abundant carbonyls and carboxyls, but a small number of hydroxyls and ether.

In the case of CBC 300, an ultra-strong peak was observed at 1057 cm^{-1} , and three comparable strong ones were also found at 1049, 1261, and 1698 cm^{-1} , which were respectively relative to $\nu(\text{C-O-C})$, $\nu(\text{C-OH})$, and $\nu(\text{C=O})$ (Ahmed et al., 2021b). It seemed to indicate a large number of ether groups, as well as plentiful carboxyls and hydroxyls in CBC 300. Correspondingly, the O 1s spectrum of CBC 300 determined an integral area ratio of 0.38: 1 for C = O: C-O, and hydroxyls and ether groups thus proved to be dominant in CBC 300 (Fig. 2d). The abundant C-O moieties in CBC 300 could be explained by the unique phenyl ether units in lignin. The aromatic majority in lignin led to a relatively stable structure and slow degradation of the corncob biochar at $300\text{ }^\circ\text{C}$. Therefore, large quantities of ether bonds remained in CBC 300.

Structural transformations of PBC and CBC were aggravated with the increasing pyrolysis temperatures. Interestingly, no significant differences were observed in the FT-IR patterns of PBC 300 and PBC 400. The similar spectra indicated a relatively stable structure in cellulose-rich PBC in the range of $300\text{ to }400\text{ }^\circ\text{C}$, which could be also demonstrated by their element analyses and XPS patterns. As listed in (Appendix A Table. S1), a series of comparable data were observed for C, N, H, and O elements in PBC 300 and PBC 400, suggesting close elemental compositions and relatively stable structures. Moreover, similar outlines were found in the survey XPS spectra of PBC 300 and PBC 400 (Fig. 2e), except for a slight decline of O 1s in PBC 400. The O 1s fine spectra also exhibited similar plots for the both biochar, indicating the stable structures. The relative stability was broken at $500\text{ }^\circ\text{C}$. After charring, some significant changes were observed in the FT-IR spectrum of PBC 500, in particular, in the fingerprint region concerning the aromatic C-H groups (Li et al., 2019; T. Zhao et al., 2019). It indicated an obvious aromatization procedure in PBC 500, which could be attributed to the varying skeleton of cellulose at high temperatures. Meanwhile, a sharp increase was found in the carbon percentage of PBC 500, followed by a corresponding decrease of oxygen content (Table 1), which also indicated intense aromatization and deoxidation reactions. Due to the drastic decomposition, some characteristic bands of metal and silicon appeared in the survey XPS analysis of PBC 500 (Fig. 2e). By contrast, CBC revealed a regular decomposition due to the stable aromatic skeleton in lignin.

3.2 U(VI) adsorption on PBC and CBC

3.2.1 Effect of pH on U(VI) adsorption

Zeta potentials of PBC and CBC were investigated to further understand the surface charge densities and adsorption abilities. As shown in Figs. 3a and 3b, the surface charge densities of PBC and CBC were decreasing with the increasing pH value. It was associated with the deprotonation of oxygenous groups retained on the biochar surface. At pH ~ 3.0, the zeta potential of PBC 300 was -10.70 mV, while, -3.25 mV for CBC 300. Obviously, more carboxyls occurred in PBC 300 in comparison with CBC 300. It was the deprotonation reaction of partial carboxyls that led to the higher negative charge in PBC 300. As pH value increased to 5.0, more carboxyls and small amounts of hydroxyls lost their protons, causing an obvious rise of surficial negative charges. Zeta potentials of PBC 300 and CBC 300 thus grew up to -26.50 and -6.61 mV, respectively. At pH ~ 7.0, all carboxyls lost the protons, and so did most of the hydroxyls. Zeta potentials thus increased to -34.70 mV for PBC 300 and -31.70 mV for CBC 300. Faster growth was observed in the zeta potentials of CBC 300 in comparison with that of PBC 300, as pH values increased from 5.0 to 7.0. It could be attributed to more hydroxyls in CBC 300 than PBC 300. Similar fast growths were also observed in zeta potentials of CBC 400 and CBC 500, indicating that plentiful hydroxyls remained in their skeletons. For CBC 400 and CBC 500, positive potentials were even determined at pH ~ 5.0, suggesting their low contents of carboxyl groups. These conclusions were consistent with the previous discussion of FT-IR and XPS analyses.

To understand the effect of pH values, the adsorption edges were performed for U(VI) adsorption on biochar. The pH values were maintained in the range of 2.0–10.0, and the contents of biochar and the initial U(VI) were 0.3 g L^{-1} and 10^{-5} M , respectively. As depicted in Figs. 3c and 3d, the adsorption of U(VI) on biochar initially increased in the pH range from 2.0 to 6.0, and then decreased gradually until pH ~ 10.0. Such phenomenon was mainly related to the changes of U(VI) species in aqueous phase and surface charge density of biochar. U(VI) existed mainly in the form of divalent cations under the acidic environment (Ahmed et al., 2021b), i.e., UO_2^{2+} . In the cases of PBC 300 and CBC 300, the electrostatic attraction was gradually strengthened between U(VI) and biochar as the pH values rose from 2.0 to 6.0, which was beneficial to the subsequent coordination reaction and thus resulted in increasing immobilization of U(VI). Above pH ~ 6.0, negatively charged species of U(VI) gradually increased, which inhibited U(VI) adsorption on biochar due to their increasing electrostatic repulsion.

Notably, close capacities were observed for U(VI) adsorption on PBC 400 and PBC 500 at pH ~ 5.0 despite the various surficial potentials. A similar phenomenon was found on three kinds of CBC in the whole pH range. These phenomena could be ascribed to the fact that the coordination interaction, rather than electrostatic attraction, dominated the surficial adsorption of U(VI).

3.2.2 Effect of initial U(VI) concentration

U(VI) adsorption on PBC and CBC were investigated in the range of U(VI) initial concentration from 0.0 to $10^{-4} \text{ mol L}^{-1}$. In the batch experiments, the contents of biochar were maintained to be 0.3 g L^{-1} , and the pH value was 5.0. As shown in Fig. 4a ~ 4b, the adsorption capacity of U(VI) rapidly rose with the

increasing initial concentration of U(VI). When U(VI) concentration exceeded 10^{-4} M, the adsorption on biochar reached equilibrium because of the saturated active sites. Maximum adsorption capacities were determined at 46.62 mg g^{-1} for PBC 300, 37.55 mg g^{-1} for PBC 400, 24.59 mg g^{-1} for PBC 500, respectively. The declined sequences in the adsorption capacities of PBC were well consistent with the decay in their surficial potentials. Under the same tested conditions, PBC showed better performances than corresponding CBC. Interestingly, CBC 300 and CBC 400, with the distinct surficial potentials, suggested similar adsorption capacities (35.60 mg g^{-1} and 33.01 mg g^{-1} , respectively). It could be attributed to the increased micropores in CBC 400 due to the enhanced decomposition. For CBC 500, adsorption property of 21.67 mg g^{-1} was determined, which was ≈ 1.64 times lower than that of CBC300. Furthermore, previous studies about biochar adsorbents were listed in Appendix A Table S3 to compare with our work. Results suggest that PBC300 and CBC300 showed the moderate efficiencies for U(VI) removal among these adsorbents, regardless of various carbon sources. As the unmodified biochar, the performances of PBC300 and CBC300 were only inferior to some carbonaceous nanofibers or modified biochars (Sun et al., 2016; Liatsou et al., 2017). Taking into account of their simple preparations and readily available sources, PBC300 and CBC300 can be regarded as excellent adsorbents of U(VI).

3.2.3 Effect of contact time

The adsorption kinetics of the biochar were also investigated. As shown in Figs. 4c and 4d, the immobilization of U(VI) was remarkably fast for all the biochar within the initial 4 h. Then, slow equilibriums were achieved at approximately 8 h. The rapid adsorption could be due to the abundant available sites on the biochar surface, i.e. carboxyls in PBC and hydroxyls in CBC (Sun et al., 2012; Lan et al., 2017; Xie et al., 2019). The latter plateau demonstrated the gradual saturation of adsorption sites on external surface (Gu et al., 2018).

The related simulation parameters of the two kinetics models were listed in (Appendix A Table. S2), and the fitting curves were also depicted in Figs. 4e and 4f. The higher R-squared value was observed for the pseudo-second-order model, indicating the better fitting degree in describing the adsorption behavior of U(VI). Moreover, the calculated q_e values from the pseudo-second-order model fittings were quite close to experimental q_e values. This demonstrated that the adsorption of U(VI) on the PBC and CBC were primarily attributed to the chemisorption (Sun et al., 2016).

3.3 Reusable performance of PBC and CBC for U(VI) adsorption

Cycle experiments were conducted to investigate the recycling of PBC 300 and CBC 300 in the natural environment. 0.1 M of Na_2CO_3 solution was chosen to act as the eluent. As presented in Appendix A Fig. S1, after six cycles of adsorption and regeneration, PBC 300 and CBC 300 maintained an approximately 88% activities with respect to initial adsorption of U(VI), which suggest quite stable structures during the adsorption and regeneration processes. The wide application should be expected in the practical treatment of wastewater containing U(VI). The slight decrease of adsorption ability for PBC 300 and CBC

300 could be due to the soft extractant, i.e., Na_2CO_3 , which was hard to extract the stable complexes of U(VI) on biochar. Therefore, the occupied adsorption sites of biochar lost the activities in the next cycles (Yoon et al., 2019; Ahmed et al., 2021b).

3.2 Adsorption mechanism of U(VI) on biochar

FT-IR and XPS analyses were performed to reveal the adsorption mechanism of U(VI) on biochar. As shown in Fig. 5a, the stretching vibration of C = O redshifted from 1696.4 cm^{-1} to 1636.8 cm^{-1} in PBC 300, while $\nu(\text{C-OH})$ in carboxyl blue-shifted from 1383.4 cm^{-1} to 1404.7 cm^{-1} . This phenomenon verified that carboxyls coordinated with U(VI) (Han et al., 2017). Moreover, a significant red-shift from 1456.4 cm^{-1} to 1413.2 cm^{-1} was observed for $\nu(\text{C-OH})$ of hydroxyls in CBC 300 (Fig. 5b), indicating the strong coordination between hydroxyls and U(VI). After being captured, $\text{U } 4f_{5/2}$ and $\text{U } 4f_{7/2}$ occurred at 392.85 eV and 382.10 eV in PBC 300, while, 393.18 eV and 382.40 eV in CBC 300 (Fig. 5c and 5d). Notably, the different binding energies of $\text{U } 4f_{5/2}$ in U(VI) species on PBC 300 and CBC 300 could be roughly ascribed to their different main coordination groups, i.e., carboxyls in PBC and hydroxyls in CBC.

O 1s fine spectra were also measured to explore the adsorption mechanism of U(VI). A new band appeared at 531.10 eV in O 1s spectra of PBC 300 and CBC 300 after the adsorption equilibrium of U(VI), which could be assigned to $\text{O} = \text{U} = \text{O}$ fraction in UO_2^{2+} (Schindler et al., 2009) (Figs. 5e and 5f). In addition, a significant shift from 531.39 to 531.15 eV occurred in the C = O moiety of PBC 300, indicating the coordination between carboxyls and U(VI). Similar red-shifts were also observed in C-O bands in CBC 300, indicating the coordination between hydroxyls and U(VI). This phenomenon could be explained that oxygen atoms in carbonyls or hydroxyls attracted partial electrons of U(VI) due to the higher electronegativity. The deviated outer electrons resulted in an increased electrostatic repulsion, and consequently reduced the binding property of the nucleus for the inner electrons (Hüfner, 2013).

4. Conclusions

In this work, a series of biochar was prepared from cellulose-rich pakchoi and lignin-rich corncob for U(VI) adsorption. The comprehensive characterizations were performed to elucidate the decomposition and evolution of biomasses at different temperatures. The adsorption equilibrium of U(VI) could be reached on all of the biochar within 8 h. The best adsorption capacity (q_e) of PBC300 was determined to be 45.62 mg g^{-1} , 1.28 times higher than that of CBC300 (35.60 mg g^{-1}), which benefitted from more carboxyls in PBC in comparison with CBC. U(VI) adsorption on PBC and CBC were mainly ascribed to the coordination interaction of oxygen-containing groups. Carboxyls in PBC and hydroxyls in CBC respectively acted as the main active sites. The significant differences in adsorption behaviors of PBC and CBC could be ascribed to the distinct evolution of cellulose and lignin. Our study proves that the readily available pakchoi biochar can act as an effective absorbent for U(VI) removal. These findings provide essential insights into understanding the oxygen-containing structural evolution and the structure-function relationship of cellulose- and lignin-rich biochar.

Declarations

Acknowledgments

This work was supported by National Natural Science Foundation of China (21876172), the “Youth Innovation Promotion Association, CAS”, Gansu Talent and Intelligence Center for Remediation of Closed and Old Deposits, and the Key Laboratory Project of Gansu Province (1309RTSA041).

Author Contributions

Yongzhong Feng: Investigation, Writing- Original draft preparation. Xiaoyi Qiu and Zhuolin Tao: Methodology. Jiayu Song: Visualization. Yaqiong Dong and Ping Li: Formal analysis. Zhengyang E, Jianjun Liang, and Qiaohui Fan: Conceptualization, Project administration, and Writing- Reviewing, Editing and Supervision. All authors commented on previous versions of the manuscript. All authors read and approved the final manuscript.

Statements & Declarations

We confirm that the manuscript is an original work, not published or under consideration for publication elsewhere, either in whole or in part. All the authors listed have approved this submission.

Competing Interests

The authors have no relevant financial or non-financial interests to disclose.

References

1. Abdel-Karim, A.-A.M., Zaki, A.A., et al., 2016. Experimental and modeling investigations of cesium and strontium adsorption onto clay of radioactive waste disposal. *Appl. Clay Sci.* 391–401.
2. Ahmed, W., Mehmood, S., Núñez-Delgado, A., et al., 2021a. Utilization of *Citrullus lanatus* L. seeds to synthesize a novel MnFe_2O_4 -biochar adsorbent for the removal of U(VI) from wastewater: Insights and comparison between modified and raw biochar. *Sci. Total Environ.* 771, 144955.
3. Ahmed, W., Mehmood, S., Núñez-Delgado, A., et al., 2021b. Fabrication, characterization and U(VI) sorption properties of a novel biochar derived from *Tribulus terrestris* via two different approaches. *Sci. Total Environ.* 780, 146617.
4. Ahmed, W., Mehmood, S., Qaswar, M., Ali, S., et al., 2021c. Oxidized biochar obtained from rice straw as adsorbent to remove U(VI) from aqueous solutions. *J. Environ. Chem. Eng.* 9, 105104.
5. Ahmed, W., Núñez-Delgado, A., Mehmood, S., et al., 2021d. Highly efficient U(VI) capture from aqueous solution by means of a hydroxyapatite-biochar nanocomposite: Adsorption behavior and

- mechanism. *Environ. Res.* 201, 111518.
6. Bradbury, A.G.W., Sakai, Y., Shafizadeh, F., 1979. A kinetic model for pyrolysis of cellulose. *J. Appl. Polym. Sci.* 23, 3271–3280.
 7. Bradbury, A.G.W., Shafizadeh, F., 1980. Chemisorption of oxygen on cellulose char. *Carbon* 18, 109–116.
 8. Cagnon, B., Py, X., Guillot, A., Stoeckli, F., Chambat, G., 2009. Contributions of hemicellulose, cellulose and lignin to the mass and the porous properties of chars and steam activated carbons from various lignocellulosic precursors. *Bioresour. Technol.* 100, 292–298.
 9. Cao, J., Xiao, G., Xu, X., Shen, D., Jin, B., 2013. Study on carbonization of lignin by TG-FTIR and high-temperature carbonization reactor. *Fuel Process. Technol.* 106, 41–47.
 10. Chen, Q., Zheng, J., Zheng, L., Dang, Z., Zhang, L., 2018. Classical theory and electron-scale view of exceptional Cd(II) adsorption onto mesoporous cellulose biochar via experimental analysis coupled with DFT calculations. *Chem. Eng. J.* 350, 1000–1009.
 11. Cheng, F., Zhang, X., Yang, X., Li, R., Wu, Y., 2021. Research on carbonization kinetic of cellulose-based materials and its application. *J. Anal. Appl. Pyrolysis* 158, 105232.
 12. Cheng, Y., He, P., Dong, F., et al., S., 2019. Polyamine and amidoxime groups modified bifunctional polyacrylonitrile-based ion exchange fibers for highly efficient extraction of U(VI) from real uranium mine water. *Chem. Eng. J.* 367, 198–207.
 13. Enders, A., Hanley, K., Whitman, T., Joseph, S., Lehmann, J., 2012. Characterization of biochars to evaluate recalcitrance and agronomic performance. *Bioresour. Technol.* 114, 644–653.
 14. Foster, R.I., Kim, K.-W., Oh, M.-K., Lee, K.-Y., 2019. Effective removal of uranium via phosphate addition for the treatment of uranium laden process effluents. *Water Res.* 158, 82–93.
 15. Gu, P., Zhang, S., Li, X., et al., 2018. Recent advances in layered double hydroxide-based nanomaterials for the removal of radionuclides from aqueous solution. *Environ. Pollut.* 240, 493–505.
 16. Han, L., Sun, H., Ro, K.S., Sun, K., Libra, J.A., Xing, B., 2017. Removal of Sb(III) and Cd(II) from aqueous solution using animal manure-derived hydrochars and pyrochars. *Bioresour. Technol.* 234, 77–85.
 17. He, Y., Luan, C., Fang, Y., Feng, X., Peng, X., Yang, G., Tsubaki, N., 2020. Low-temperature direct conversion of methane to methanol over carbon materials supported Pd-Au nanoparticles. *Catal. Today* 339, 48–53.
 18. Inyang, M.I., Gao, B., Yao, Y., et al., 2016. A review of biochar as a low-cost adsorbent for aqueous heavy metal removal. *Crit. Rev. Environ. Sci. Technol.* 46, 406–433.
 19. Ishimaru, K., Hata, T., Bronsveld, P., Meier, D., Imamura, Y., 2007. Spectroscopic analysis of carbonization behavior of wood, cellulose and lignin. *J. Mater. Sci.* 42, 122–129.
 20. Jin, J., Li, S., Peng, X., Liu, W., et al., 2018. HNO₃ modified biochars for U(VI) removal from aqueous solution. *Bioresour. Technol.* 256, 247–253.

21. Kijima, M., Hirukawa, T., Hanawa, F., Hata, T., 2011. Thermal conversion of alkaline lignin and its structured derivatives to porous carbonized materials. *Bioresour. Technol.* 102, 6279–6285.
22. Komnitsas, K., Zaharaki, D., Bartzas, G., Kaliakatsou, G., Kritikaki, A., 2016. Efficiency of pecan shells and sawdust biochar on Pb and Cu adsorption. *Desalin. Water Treat.* 57, 3237–3246.
23. Kumar, S., Loganathan, V.A., Gupta, R.B., Barnett, M.O., 2011. An assessment of U(VI) removal from groundwater using biochar produced from hydrothermal carbonization. *J. Environ. Manage.* 92 (10), 2504–2512.
24. Lan, J.-H., Chai, Z.-F., Shi, W.-Q., 2017. A combined DFT and molecular dynamics study of U(VI)/calcite interaction in aqueous solution. *Sci. Bull.* 62, 1064–1073.
25. Li, J., Li, Y., Wu, Y., Zheng, M., 2014. A comparison of biochars from lignin, cellulose and wood as the sorbent to an aromatic pollutant. *J. Hazard. Mater.* 280, 450–457.
26. Li, M., Liu, H., Chen, T., Dong, C., Sun, Y., 2019. Synthesis of magnetic biochar composites for enhanced U(VI) adsorption. *Sci. Total Environ.* 651, 1020–1028.
27. Li, N., Yin, M., Tsang, D.C.W., et al., 2019. Mechanisms of U(VI) removal by biochar derived from ficus microcarpa aerial root: A comparison between raw and modified biochar. *Sci. Total Environ.* 697, 134115.
28. Li, P., Wang, J., Wang, Y., et al., 2019a. Photoconversion of U(VI) by TiO₂: An efficient strategy for seawater uranium extraction. *Chem. Eng. J.* 365, 231–241.
29. Li, P., Wang, J., Wang, Y., et al., 2019b. An overview and recent progress in the heterogeneous photocatalytic reduction of U(VI). *J. Photochem. Photobiol. C Photochem. Rev.* 41, 100320.
30. Liu, H., Li, M., Chen, T., Chen, C., et al., 2017. New synthesis of nZVI/C composites as an efficient adsorbent for the uptake of U(VI) from aqueous solutions. *Environ. Sci. Technol.* 51, 9227–9234.
31. Liu, X., Xu, X., Sun, J., Alsaedi, A., Hayat, T., Li, J., Wang, X., 2018. Insight into the impact of interaction between attapulgite and graphene oxide on the adsorption of U(VI). *Chem. Eng. J.* 343, 217–224.
32. Liatsou, I., Michail, G., Demetriou, M., Pashalidis, I., 2017. Uranium binding by biochar fibres derived from *Luffa cylindrica* after controlled surface oxidation. *J. Radioanal. Nucl. Chem.* 311, 871–875.
33. Lu, S., Hu, J., Chen, C., Chen, X., Gong, Y., Sun, Y., Tan, X., 2017. Spectroscopic and modeling investigation of efficient removal of U(VI) on a novel magnesium silicate/diatomite. *Sep. Purif. Technol.* 174 425–431.
34. Mellah, A., Chegrouche, S., Barkat, M., 2006. The removal of U(VI) from aqueous solutions onto activated carbon: Kinetic and thermodynamic investigations. *J. Colloid Interface Sci.* 296, 434–441.
35. Meng, Y., Contescu, C.I., Liu, P., Wang, S., Lee, S.-H., Guo, J., Young, T.M., 2021. Understanding the local structure of disordered carbons from cellulose and lignin. *Wood Sci. Technol.* 55, 587–606.
36. Philippou, K., Anastopoulos, I., Dosche, C., Pashalidis, I., 2019. Synthesis and characterization of a novel Fe₃O₄-loaded oxidized biochar from pine needles and its application for uranium removal. Kinetic, thermodynamic, and mechanistic analysis. *J. Environ. Manage.* 252, 109677.

38. Prabhu, D.R., Mohapatra, P.K., Raut, D.R., Pathak, P., Billard, I., 2017. Extraction of U(VI) from nitric acid solutions using N,N-dihexyloctanamide in ionic liquids: Solvent extraction and spectroscopic studies. *Solvent Extr. Ion Exch.* 35, 423–438.
39. Rey-Raap, N., Ribeiro, L.S., Órfão, J.J. de M., Figueiredo, J.L., Pereira, M.F.R., 2019. Catalytic conversion of cellulose to sorbitol over Ru supported on biomass-derived carbon-based materials. *Appl. Catal. B Environ.* 256, 117826.
40. Schindler, M., Hawthorne, F.C., Freund, M.S., Burns, P.C., 2009. XPS spectra of uranyl minerals and synthetic uranyl compounds. II: The O 1s spectrum. *Geochim. Cosmochim. Acta.* 73, 2488–2509.
41. Shafizadeh, F., Furneaux, R.H., Cochran, T.G., Scholl, J.P., Sakai, Y., 1979. Production of levoglucosan and glucose from pyrolysis of cellulosic materials. *J. Appl. Polym. Sci.* 23, 3525–3539.
42. Shafizadeh, F., Lai, Y.-Z., 1975. Thermal degradation of 2-deoxy-D-arabino-hexonic acid and 3-deoxy-D-ribo-hexono-1,4-lactone. *Carbohydr. Res.* 42, 39–53.
43. Shafizadeh, F., Sekiguchi, Y., 1984. Oxidation of chars during smoldering combustion of cellulosic materials. *Combust. Flame.* 55, 171–179.
44. Sharma, R.K., Wooten, J.B., Baliga, V.L., et al., 2004. Characterization of chars from pyrolysis of lignin. *Fuel* 83, 1469–1482.
45. Hiifner, S. 2003. *Photoelectron Spectroscopy Principles and Applications*, Third ed., Springer Science & Business Media, New York.
46. Suliman, W., Harsh, J.B., Abu-Lail, N.I., Fortuna, A.-M., Dallmeyer, I., Garcia-Perez, M., 2016. Influence of feedstock source and pyrolysis temperature on biochar bulk and surface properties. *Biomass Bioenerg.* 84, 37–48.
47. Sun, Y., Wu, Z.Y., Wang, X., Ding, C., Cheng, W., Yu, S.H., Wang, X., 2016. Macroscopic and microscopic investigation of U(VI) and Eu(III) adsorption on carbonaceous nanofibers. *Environ. Sci. Technol.* 50, 4459–4467.
48. Sun, Y., Yang, S., Sheng, G., Guo, Z., Wang, X., 2012. The removal of U(VI) from aqueous solution by oxidized multiwalled carbon nanotubes. *J. Environ. Radioact.* 105, 40–47.
49. Suzuki, T., Yamada, T., Okazaki, N., Tada, A., Nakanishi, M., Futamata, M., Chen, H.-T., 2001. Electromagnetic shielding capacity of wood char loaded with nickel. *Mater. Sci. Res. Int.* 7, 206–212.
50. Wang, J., Wang, Y., Wang, W., et al., 2020a. Tunable mesoporous g-C₃N₄ nanosheets as a metal-free catalyst for enhanced visible-light-driven photocatalytic reduction of U(VI). *Chem. Eng. J.* 383, 123193.
51. Wang, J., Wang, Y., Wang, W., et al., 2020b. Visible light driven Ti³⁺ self-doped TiO₂ for adsorption-photocatalysis of aqueous U(VI). *Environ. Pollut.* 262, 114373.
52. Wang, Y., Wang, J., Wang, J., et al., 2020. Efficient recovery of uranium from saline lake brine through photocatalytic reduction. *J. Mol. Liq.* 308, 113007.
53. Wen, T., Wang, X., Wang, J., et al., 2016. A strategically designed porous magnetic N-doped Fe/Fe₃C@C matrix and its highly efficient U(VI) remediation. *Inorg. Chem. Front.* 3, 1227–1235.

54. Wu, F., Chen, L., Hu, P., Wang, Y., Deng, J., Mi, B., 2021. Industrial alkali lignin-derived biochar as highly efficient and low-cost adsorption material for Pb(II) from aquatic environment. *Bioresour. Technol.* 322, 124539.
55. Wu, Y., Chen, D., Kong, L., Tsang, D.C.W., Su, M., 2019. Rapid and effective removal of U(VI) from aqueous solution by facile synthesized hierarchical hollow hydroxyapatite microspheres. *J. Hazard. Mater.* 371, 397–405.
56. Xie, X., Goodell, B., Zhang, D., Nagle, D.C., et al., 2009. Characterization of carbons derived from cellulose and lignin and their oxidative behavior. *Bioresour. Technol.* 100, 1797–1802.
57. Xie, Y., Chen, C., Ren, X., Wang, X., Wang, H., Wang, X., 2019. Emerging natural and tailored materials for uranium-contaminated water treatment and environmental remediation. *Prog. Mater. Sci.* 103, 180–234.
58. Xu, Z., Xing, Y., Ren, A., Ma, D., Li, Y., Hu, S., 2020. Study on adsorption properties of water hyacinth-derived biochar for U(VI). *J. Radioanal. Nucl. Chem.* 324, 1317–1327.
59. Yang, H., Yan, R., Chen, H., Lee, D.H., Zheng, C., 2007. Characteristics of hemicellulose, cellulose and lignin pyrolysis. *Fuel* 86, 1781–1788.
60. Yoon, K., Cho, D.-W., Tsang, Y.F., Tsang, D.C.W., Kwon, E. E., Song, H., 2019. Synthesis of functionalised biochar using red mud, lignin, and carbon dioxide as raw materials. *Chem. Eng. J.* 361, 1597-1604.
61. Zhang, Q., Wang, Y., Wang, Z., Zhang, Z., Wang, X., Yang, Z., 2021. Active biochar support nano zero-valent iron for efficient removal of U(VI) from sewage water. *J. Alloys Compd.* 852, 156993.
62. Zhao, T., Tang, Z., Zhao, X., Zhang, H., Wang, J., Wu, F., Giesy, J.P., Shi, J., 2019. Efficient removal of both Sb(III) and Sb(V) from environmental water using titanate nanotubes and nanoparticles. *Environ. Sci. Nano* 6, 834–850.
63. Zhao, Y., Liu, Y., Du, J., Zhang, X., et al., 2019. Facile synthesis of interconnected carbon network decorated with Co_3O_4 nanoparticles for potential supercapacitor applications. *Appl. Surf. Sci.* 487, 442–451.

Figures

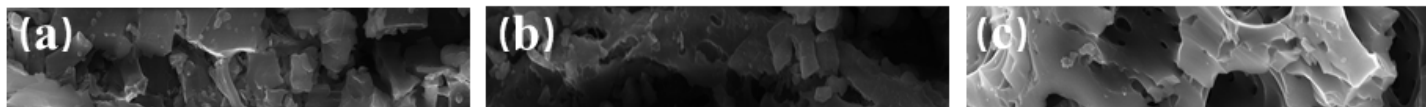


Figure 1

SEM images of PBC 300, 400, 500 (a, b, c) and CBC 300, 400, 500 (d, e, f).

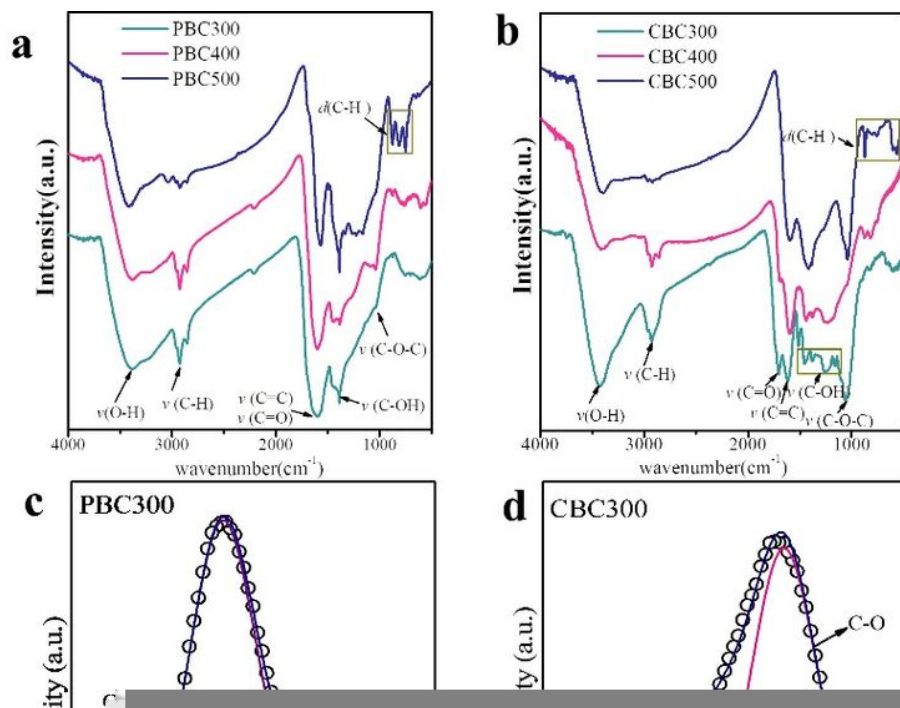


Figure 2

FT-IR spectra and survey XPS spectra of PBC (a, e) and CBC (b, f), O 1s high-resolution XPS spectrum of PBC 300 (c) and CBC 300 (d) without water washing.

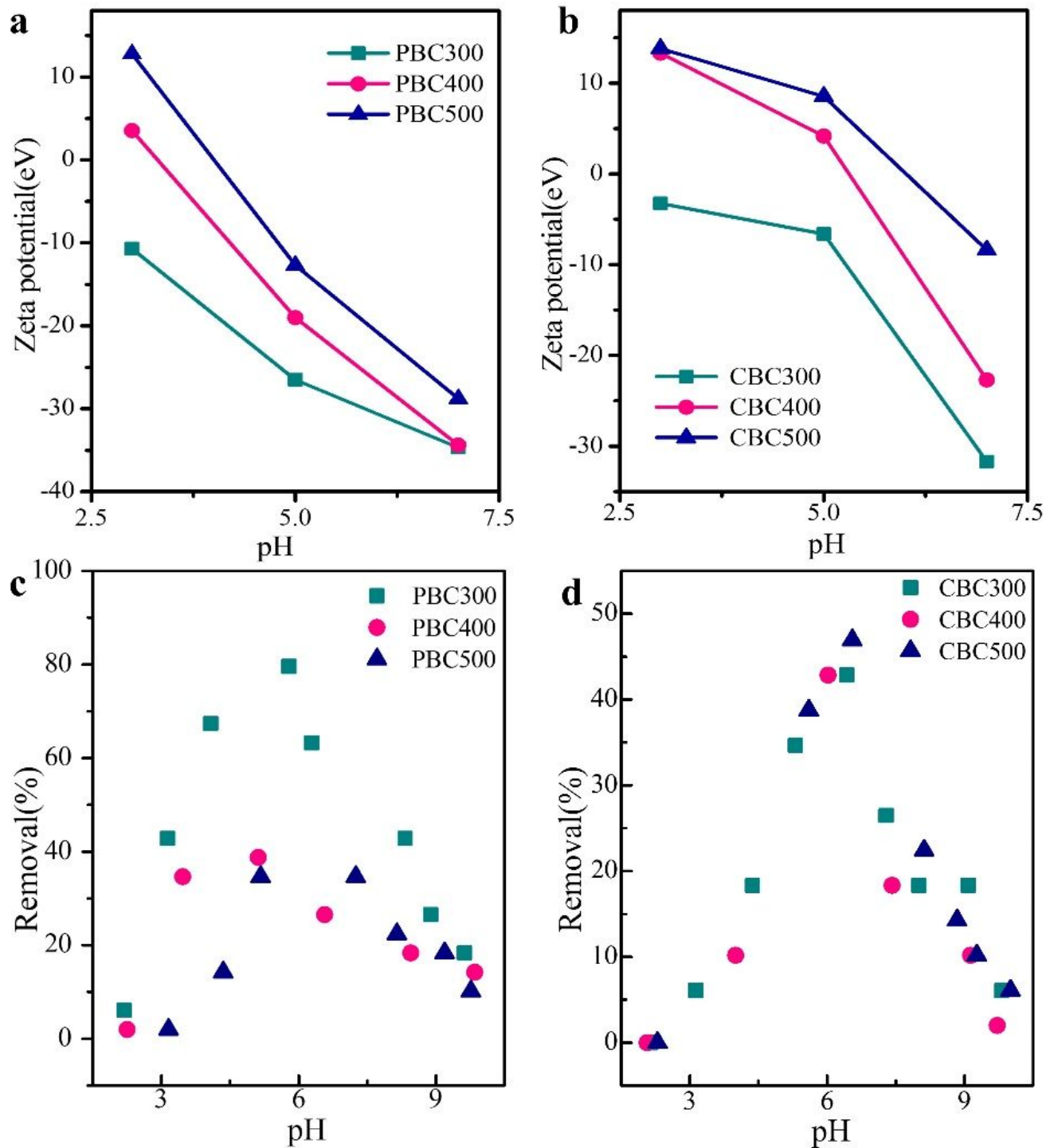


Figure 3

Zeta potential and impacts of pH values on U(VI) adsorption on a series of PBC (a, c) and CBC (b, c) ($T=298\text{K}$, $m/v=0.3\text{g L}^{-1}$, $C_0=1.0\times 10^{-5}\text{ M}$).

Figure 4

Effect of initial concentration, time on adsorption capacity and pseudo-second sorption model of PBC (a, c, e) and CBC (b, d, f) ($T=298\text{K}$, $m/v=0.3\text{g L}^{-1}$, $\text{pH}=5.0$).

Figure 5

FT-IR and O 1s high resolution XPS spectra of PBC 300 (a, e) and CBC 300 (b, f) before and after U(VI) loading (the bottom patterns were collected from the biochar immersed in the solution of background electrolyte), U 4f high resolution XPS spectrum of PBC 300 (c) and CBC 300 (d).

Supplementary Files

This is a list of supplementary files associated with this preprint. Click to download.

- [Supplementarydata202232.docx](#)